The influence of crosswind tidal currents on Langmuir circulation in a shallow ocean

T. Kukulka,[1] A. J. Plueddemann,[2] J. H. Trowbridge,[3] and P. P. Sullivan[4]

Received 18 January 2011; revised 31 March 2011; accepted 3 May 2011; published 4 August 2011.

[1] Langmuir circulation (LC) is a turbulent process driven by wind and surface waves that plays a key role in transferring momentum, heat, and mass in the oceanic surface layer. On the coastal shelves the largest-scale LC span the whole water column and thus couple the surface and bottom boundary layers and enhance turbulent mixing. Observations and large eddy simulations (LES) of a shallow coastal ocean demonstrate that these relatively large scale Langmuir cells are strongly influenced by crosswind tidal currents. Two mechanisms by which crosswind tidal shear may distort and disrupt Langmuir cells are proposed. The first mechanism involves cell shearing due to differential advection across the whole cell. For the second mechanism, middepth vertical LC currents advect sheared mean crosswind current, leading to the attraction of upwelling and downwelling regions, so that LC cells are unsustainable when both regions overlap. Scaling arguments indicate that LC cells are more susceptible to crosswind shear distortion for smaller LC surface velocity convergence and greater cell aspect ratio (vertical to horizontal LC scale), which is consistent with the results obtained from the observations and LES. These results imply that scaling of LC characteristics in a coastal ocean differs from that in the open ocean, which has important practical implications for parameterizing enhanced mixing due to LC.

Citation: Kukulka, T., A. J. Plueddemann, J. H. Trowbridge, and P. P. Sullivan (2011), The influence of crosswind tidal currents on Langmuir circulation in a shallow ocean, *J. Geophys. Res.*, *116*, C08005, doi:10.1029/2011JC006971.

1. Introduction

[2] Langmuir circulation (LC) is a key turbulent processes in the upper ocean [*Leibovich*, 1983; *Thorpe*, 2004]. LC enhances air-sea exchange and mixing in the ocean surface boundary layer. Previous investigations support an LC generation mechanism based on wave-current interactions as described in the systematic mathematical theory by *Craik and Leibovich* [1976]. An integral component of this mechanism is the Stokes drift due to surface gravity waves, which tilts vertical vorticity into the direction of wave propagation to form wind-aligned roll vortices.

[3] Recent investigations indicate that LC also plays a key role in mixing processes in a coastal, shallow ocean [*Gargett et al.*, 2004; *Gargett and Wells*, 2007; *Tejada-Martínez and Grosch*, 2007]. Many LC characteristics agree with former descriptions of Langmuir circulations in deep water, such as the three-dimensional structure of the velocity field. Unlike deep water LC, however, observations and simulations show that LC can extend throughout the whole water column in a shallow ocean [*Gargett et al.*, 2004]. Such LCs were termed "Langmuir supercells" with crosswind scale (distance between convergence zones) three to six times the water depth. Strong near-bottom intensification of the along-wind velocity jets are typically located below downwelling regions and contribute to sediment resuspension. This jet was captured in the shallow water large eddy simulation (LES) model based on the Craik-Leibovich equations [*Tejada-Martínez and Grosch*, 2007]. These LES results clearly highlight the differences between pure shear-driven flow and flow that also includes Stokes drift forcing to generate LC. These previous studies of Langmuir turbulence in shallow water did not focus on tidal effects.

[4] The goal of this paper is to provide evidence that crosswind tidal flow can significantly alter LC characteristics in a coastal ocean. In section 2, we will review the observational and numerical methodology. Observations show a modulation of LC strength in the presence of crosswind tidal currents, with LC strength decreasing as current magnitude increases (section 3). Prompted by these observations, we propose two LC distortion mechanisms (section 4),which are tested based on a large eddy simulation model (section 5). Our results have important implica-

[1]Physical Ocean Science and Engineering, College of Earth, Ocean, and Environment, University of Delaware, Newark, Delaware, USA.
[2]Department of Physical Oceanography, Woods Hole Oceanographic Institution, Woods Hole, Massachusetts, USA.
[3]Department of Applied Ocean Physics and Engineering, Woods Hole Oceanographic Institution, Woods Hole, Massachusetts, USA.
[4]National Center for Atmospheric Research, Boulder, Colorado, USA.

0148-0227/11/2011JC006971

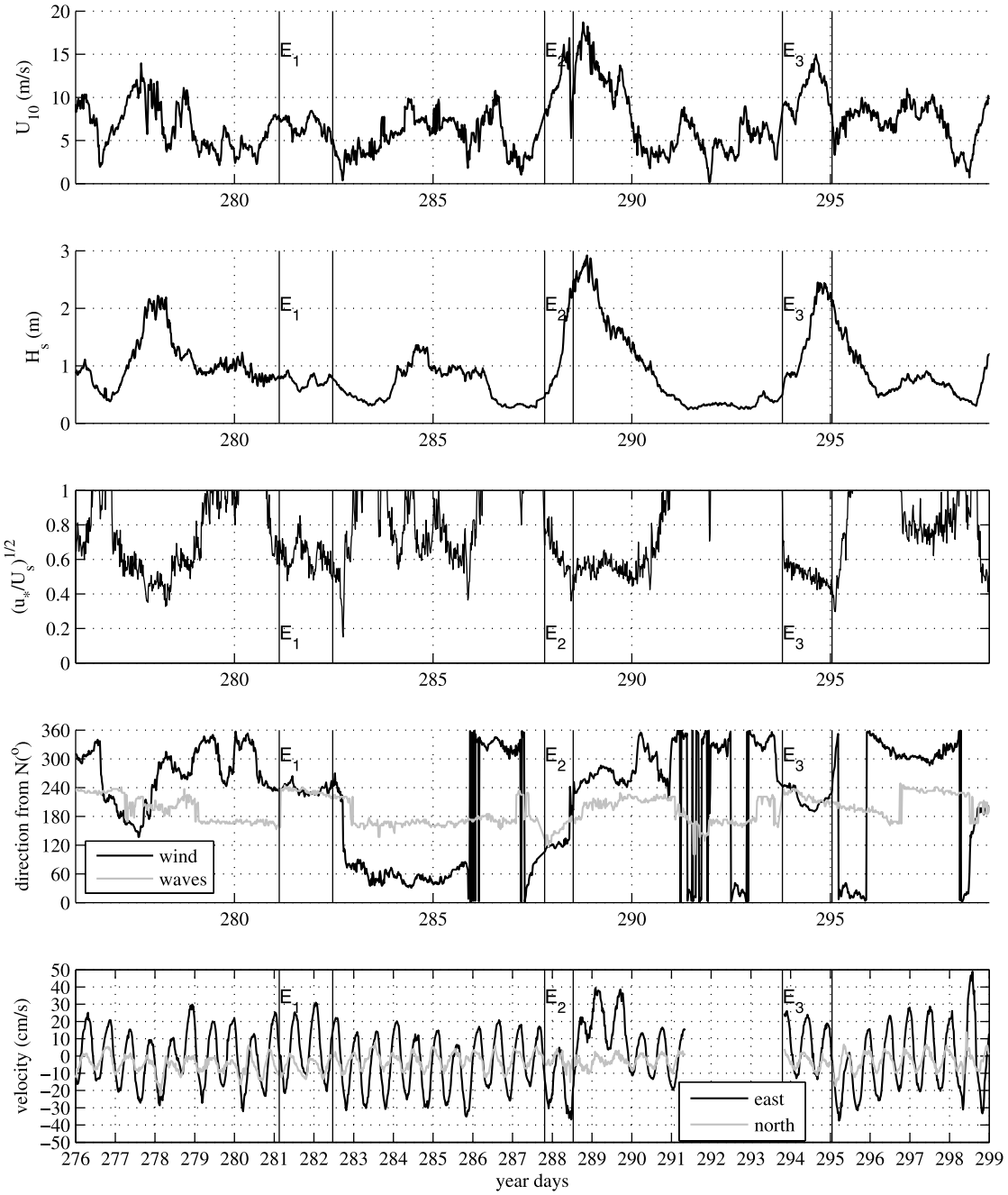

Figure 1. Wind, wave, and tidal conditions during the second fan beam deployment. U_{10}, wind speed at 10 m height; H_s, significant wave height. Langmuir turbulence is expected for a small turbulent Langmuir number, say, $\sqrt{u*/U_s} < 0.7$. The wind and wave angle convention is such that 0° is from north and angles increase clockwise, so that 270° is from the west. The fifth panel shows averaged velocities between 2 m and 8 m depth. Events (E) are defined such that $U_{10} > 5$ m/s and all events are at least 6 h long with wind and wave directions aligned within 45°.

tions for scaling LC in a coastal ocean and for understanding LC in complex conditions as outlined in section 6.

2. Methods

2.1. Observations

2.1.1. CBLAST-low Experiment

[5] The Coupled Boundary Layers and Air-Sea Transfer Experiment in Low Winds (CBLAST-low) was conducted on the west Atlantic continental shelf about 3 km south of Martha's Vineyard, MA, USA, during 2001 and 2003 [*Edson et al.*, 2007; *Gerbi et al.*, 2009]. The water depth, H, of the study site was roughly $H = 16$ m. The CLBAST-low data set provides comprehensive measurements of a) two-dimensional ocean surface wavefields [*Churchill et al.*, 2006]; b) heat and momentum air-sea fluxes; c) vertical profiles of temperature, salinity, and currents; as well as

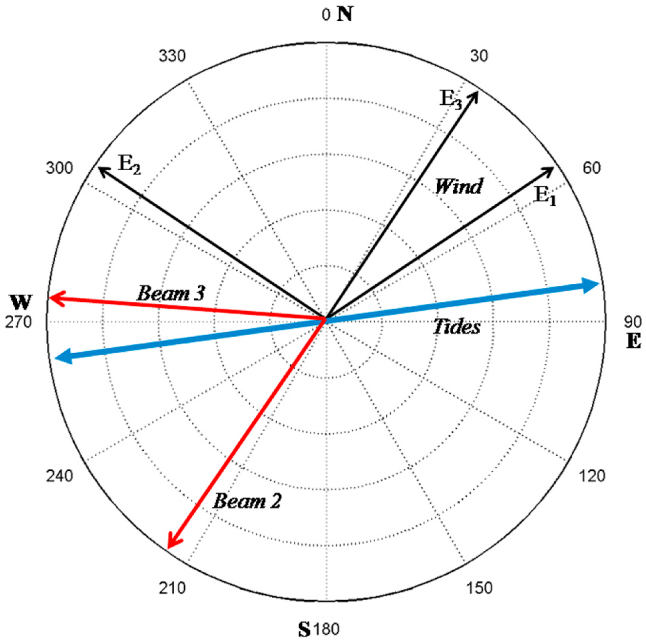

Figure 2. Wind directions (averaged for each event), principal tidal axis, and instrument beam directions for beams 2 and 3.

d) unique subsurface turbulence estimates from "fanbeam LC detectors" [*Plueddemann et al.*, 2001].

[6] This fan beam instrument consists of special purpose acoustic Doppler current profiler (ADCP) that measures horizontal velocities of surface trapped bubbles [*Smith*, 1989; *Zedel and Farmer*, 1991]. In the presence of LC, sonar beams oriented perpendicular to the wind direction (crosswind) detect horizontal bands due to velocity convergence zones of coherent surface LC structures.

[7] The analysis presented here is based on the fan beam deployment from the end of September to beginning of November of 2003, when wind, wave, and current conditions where generally complex with turning winds, non-equilibrium seas, and tides (Figure 1). Tidal currents are dominantly semidiurnal and oscillate approximately east and west along the south shore of Martha's Vineyard with a maximum amplitude of about 0.3 m/s. Water column velocity profiles were measured with two upward looking ADCPs [*Gerbi et al.*, 2009]. In this study, only data from the bottom-mounted ADCP were used. This instrument profiled from approximately 2 m above the bottom to 3 m below the surface with 0.5 m vertical bins. Buoyancy surface forcing likely plays a secondary role in the turbulence dynamics during the analysis period, since the magnitude of the Monin-Obukhov length is usually much larger than the ocean depth.

[8] Measured density differences between depths at 1.4 m and 11.9 m are generally also small (below 0.02 kg m^{-3}) during most of the analysis period, so that stratification effects are likely dynamically insignificant. A relatively small turbulent Langmuir number, $La_t = \sqrt{u*/U_s}$, where $u*$ is the water surface friction velocity and U_s is the surface Stokes drift, indicates that LC effects are significant [*McWilliams et al.*, 1997].

2.1.2. Events With Aligned Wind and Waves

[9] To reduce the complexity of the problem, we will focus our analysis on wind driven seas, i.e., on periods when the winds are at least moderate (wind speeds at 10 m height, U_{10} exceed 5 m/s) and winds and waves are approximately aligned (misalignment angle between the two is below 45°). We furthermore require that analysis periods are long enough so that tidal variations can be observed in the fan beam signal. This selection criterion reduces the data set to three distinct events, lasting between 18 h and 31 h (Figure 1). During these events, La_t is usually between 0.4 and 0.7 (Figure 1, third panel). Note that La_t is larger than typical open ocean La_t with $La_t \approx 0.3$. According to the regime diagram by *Li et al.* [2005] open ocean Langmuir turbulence is expected for $La_t < 0.7$, which is confirmed for coastal oceans by LC LES of *Tejada-Martínez and Grosch* [2007] with $La_t = 0.7$. During the first, second, and third events (E1, E2, and E3, respectively) the mean wind directions are from WSW (240°), ESE (120°), and SSW (210°), respectively (Figure 2). For the first event, wind and wave conditions are relatively steady, with $U_{10} = 5$ to 8.5 ms^{-1} and a significant wave height H_s between 0.5 and 1.0 m. During the second and third event winds increase from $U_{10} = 5$ to 15 ms^{-1} and wavefields develop from $H_s \approx 0.5$ m to 2.5 m. At the end of both events the wind drops back to 5 m/s.

2.1.3. Fan Beam Observations

[10] In order to compare measurements with model results, it is necessary to understand the vertical extent of the surface measurements. The near surface bubble distribution decreases roughly exponentially in the vertical with a decay scale around 1.0 to 1.5 m and confines the vertical extent of the measurement volume to about 3 m, depending on wind and wave conditions [*Plueddemann et al.*, 2001]. Maximum horizontal range along the surface also varies with wind and wave conditions [*Plueddemann et al.*, 2001]. For this study, a conservative, fixed aperture of 85 m was used with "range cells" along the sea surface with dimensions of about 2.4 m along beam and 5 m cross beam. The limited along beam extent implies that spatial scales significantly longer than 85 m are undetectable by the fan beam. The fan beam ping rate was 1 Hz, with 56 ping ensembles recorded every minute.

[11] Postprocessing was applied to average over surface wave orbital velocities [*Smith*, 1992] and to extract a robust signal of near-surface velocity convergence regions from the noisy acoustic measurements [see also *Gerbi et al.*, 2009]. Based on conservative quality control criteria, only beam two and three were processed for ranges between 37 m and 123 m (bin 9 to 45). During the three analysis events beams two and three were approximately directed toward SSW (210°) and W (270°), respectively (Figure 2). The instantaneous angle between the beams and LC convergence zones (assumed to be oriented with the wind) typically exceeds 45° and is never below 30°, so that a significant fraction of surface convergence velocities are along beam. Each beam was processed separately to produce a velocity anomaly for 20 min time intervals. A temporal high-pass filter with a half-power point at 40 min was first applied to remove the tidal variability that dominated the raw velocities. The high-passed velocities were then detrended in time and range within contiguous 20 min processing windows. To capture only the largest scales, a moving average with a

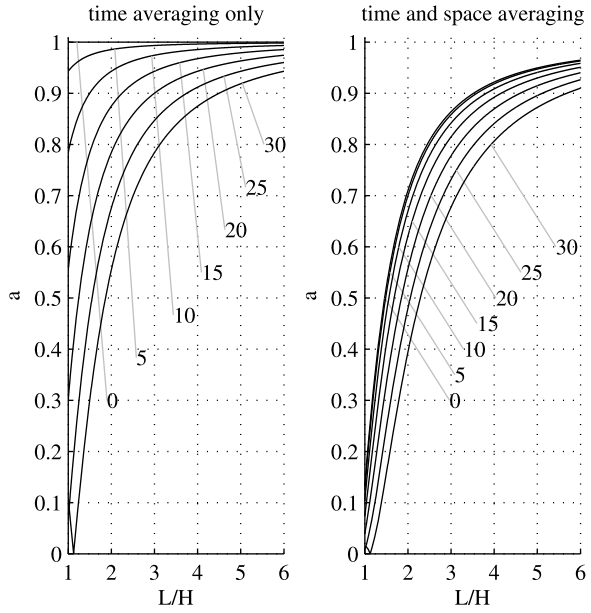

Figure 3. Filter attenuation coefficient a from (1) as a function of horizontal spatial scale for along-beam advection speeds V from 0 to 30 cm/s in 5 cm/s intervals (a decreases with V): (left) a_{time} and (right) a_{total} for a 14 m filter length, as discussed in section 2.1.4.

window length of 14 m was further applied. This final filtered velocity anomaly is denoted by v'. The root mean square of this quantity, based on 20 min contiguous intervals, denoted vrms, was recorded for each beam.

[12] It is important to recognize that spatial features with horizontal scales smaller than, say, two times the water depth or 32 m, can be attenuated significantly by the post-processing described above. Thus, the vrms values presented here capture only the large-scale features that one anticipates in the presence of well developed Langmuir cells. Details of the attenuation due to averaging depend on the mean advection speed, as discussed in section 2.1.4.

2.1.4. Fan Beam Scale Response

[13] Because of the applied spatial and temporal averaging procedures, the fan beam vrms captures only relatively long spatial scales. We will consider the effect of temporal averaging in the presence of an advection velocity V followed by combined time-space averaging. An oscillatory signal with unit amplitude and radian frequency (or wave number) ω is attenuated by the factor a due to the moving average filter operation. For a filter of duration (or spatial length) T, a is

$$a(\omega, T) = \frac{1}{T}\left|\int_0^T \exp(i\omega t)dt\right| = \frac{\sqrt{2}}{\omega T}\sqrt{1-\cos(\omega T)}. \quad (1)$$

Therefore, any feature with horizontal spatial scale L that is advected with a velocity V is attenuated by $a_{\text{time}} = a(\omega, T)$, where $\omega = 2\pi V/L$ and $T = 60$ s, consistent with the internal temporal fan beam averaging. Clearly, shorter scales are attenuated by tidal advection for larger V (Figure 3, left). Because shorter scales are also attenuated by spatial averaging, the total attenuation resulting from both spatial and temporal averaging is lessdependent on along-beam advection (Figure 3, right). Since the filters are linear, the total attenuation can be written as

$$a_{\text{total}} = a_{\text{time}} \times a_{\text{space}} \quad (2)$$

where $a_{\text{space}} = a(\omega, T)$ with filter length $T = 14$ m and $\omega = 2\pi L$. For a typical range of observed tidal speeds (between 0 and 0.3 m/s) the half power point of the measured fan beam vrms (at $a_{\text{total}} = 2^{-1/2} \approx 0.7$) is roughly between $L/H \approx 2 - 3$. The fan beam scale response improves for relatively large and organized LC motions. For along-beam advection speeds between 0.2 and 0.3 m/s and LC spacing of $L/H \approx 3 - 4$, that have been observed during the wind events, we anticipate attenuations between 6% and 22% (Table 1).

[14] Implications for the observed fan beam vrms during the three wind events will be explained further below.

2.2. Model

[15] In order to model LC in a shallow ocean with mean currents we modify a laterally periodic large eddy simulation model for the open ocean [*McWilliams et al.*, 1997]. The open ocean model solves the CL equation spatially averaged over the subgrid scale (SGS). The CL momentum equations capture LC dynamics by a vortex force that involves the Stokes drift. The mean flow is generated by constant large-scale pressure gradients similar to the procedure by *Li et al.* [2004]. Unlike an open ocean model, we implement solid wall boundary conditions at the ocean bottom following the atmospheric approach from *Sullivan et al.* [1994]. Turbulent SGS fluxes are parameterized via an SGS eddy viscosity that depends on the SGS turbulent kinetic energy (TKE). The SGS TKE, in turn, is determined from a prognostic equation [*Deardorff*, 1973]. Closer to the boundaries the SGS model is modified for better correspondence with Monin-Obukhov similarity theory [*Sullivan et al.*, 1994]. Earth rotation (Coriolis force) is not included in our model, similar to the study by *Tejada-Martínez and Grosch* [2007]. Our coastal LES model has been tested to reproduce a) logarithmic velocity layers close to the boundaries (without crosswind mean flow and LC), b) shallow-water LC (without crosswind mean flow) similar to the work of *Tejada-Martínez and Grosch* [2007], and c) flow and turbulence characteristics of open channel flow (with pressure gradient driven mean flow, but without wind stress and LC) [*Nezu*, 2005]. Like *Tejada-Martínez and Grosch* [2007], we find that the log layer near the bottom boundary is disrupted in the presence of LCs that extend throughout the water column. However, for distances more than 1 m away from the boundaries, the simulations resolve over 90% of the flux and energy carrying eddies, so that the LES results presented here are "well resolved" and depend only weakly on the details of the SGS parameterization [*Pope*, 2008].

Table 1. Expected Fan Beam vrms Attenuation Based on (2)

V (m/s)	L/H	Attenuation (%)
0.2	3	10
0.2	4	6
0.3	3	22
0.3	4	12

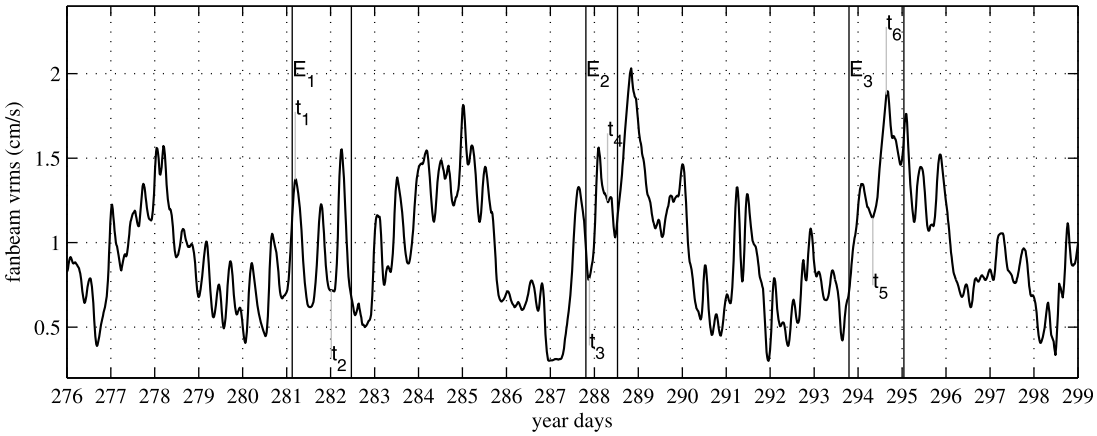

Figure 4. Fan beam vrms determined from beams 2 and 3. For each time t_1 to t_6 measured velocity anomalies are shown in Figure 6. Typically, these times have been chosen to show one instance of relatively large vrms and one instance of relatively small vrms during each event (events are defined in Figure 1).

[16] To illustrate the effects of crosswind mean flow on LC, we study nearly stationary LES solutions for different wind and wave forcing and different crosswind mean flows, the latter are generated by a crosswind pressure gradient.

[17] The mean pressure gradient can be estimated based on the horizontally averaged crosswind momentum equation

$$0 = -\frac{\partial P}{\partial y} + \frac{\partial}{\partial z}\left\langle \tau_{yz}^{\mathrm{SGS}} - \rho vw \right\rangle, \tag{3}$$

where ρ is the water density, $\partial P/\partial y$ is the large-scale crosswind pressure gradient, z, y are the vertical and crosswind coordinates, respectively, $\langle\cdot\rangle$ indicates horizontal averages, v, w are the resolved crosswind and vertical velocities, respectively, and τ_{yz}^{SGS} is the y, z component of the subgrid-scale stress tensor. Integration of (3) over the water column results in

$$0 = -H\frac{\partial P}{\partial y} + \tau_{yz}^{\mathrm{surf}} - \tau_{yz}^{\mathrm{bot}}, \tag{4}$$

where $\tau_{yz}^{\mathrm{surf}}$ and τ_{yz}^{bot} denote the crosswind surface and bottom stresses, respectively. The bottom stress is parameterized by $\tau_{yz}^{\mathrm{bot}} = c_D V\sqrt{V^2 + U^2}$, with $V = \langle v\rangle$, $U = \langle u\rangle$ and c_D is a suitable drag coefficient.

[18] The drag coefficient has been determined based on a best fit for direct covariance measurements of Reynolds stresses at $z = 0.75$ m above bottom, where $c_D = 0.0034$ (J. H. Trowbridge, personal communication, 2011). During the measurement period, stress and dissipation estimates were roughly consistent with a constant-stress logarithmic layer, so that c_D can be expressed in terms of a roughness length of $z_0 = 0.75\ \mathrm{m} \times \exp(-\kappa/\sqrt{c_D}) \approx 0.001$ m ($\kappa = 0.4$ is the von Karman constant). Consistent with the Reynolds stress measurements from the study site, we employ a roughness length of $z_0 = 0.001$ m in our LES model to relate the local near bottom velocities to local bottom stresses.

[19] For the simulations with crosswind mean flow $\partial P/\partial y$ is chosen, so that V at middepth is about ~20 cms^{-1}. The total ocean depth is $H = 16$ m consistent with CBLAST-low observations with 100 vertical grid points. The horizontal domain is 96 m × 96 m with 256 × 256 grid points. The Stokes drift was imposed based on a monochromatic surface wave with a significant wave height and frequency (wavelength) consistent with observations. The full dispersion relation with depth effects was used to calculate the Stokes drift. The wavelength λ was kept fixed at 40 m, which corresponds roughly to 5s waves periods. Generally, the Stokes drift decay with depth (related to λ) plays a significant dynamical role [*Polton and Belcher*, 2007; *Harcourt and D'Asaro*, 2008], but is not further investigated in this study as $\lambda = 40$ *m* represents a typical value for the wind-driven part of the observed wave spectrum [*Churchill et al.*, 2006].

3. Observed Tidal Influence on LC

3.1. Fan Beam vrms

[20] During the fan beam deployment period the vrms signal varies irregularly over a range of time scales, reflecting the complex environmental forcing conditions that drive upper ocean turbulence (Figure 4). Noticeably, a tidal signature appears to be superimposed on the subtidal frequency variations (compare with tidal currents in Figure 1). E.g., a ~12 h oscillation is embedded when vrms values increase during a storm event from year day 287 to about year day 289, coinciding with event E2. As discussed in section 2.1.4, a tidal attenuation in the vrms signal somewhere between 6% and 22% is anticipated due to the internal temporal averaging of the instrument for observed scales between $L/H \sim 3 - 4$ (see section 3.2). However, consecutive vrms peaks and troughs frequently change by more than 30%, so that it is unlikely that these tidal variations are solely due to the instrument response.

[21] In order to investigate this tidal variation further, it is useful to consider the likely LC orientation relative to wind, waves, tide, and instrument beam directions. Linear stability analysis suggests that LC convergence zones are oriented in the directions where the near surface Eulerian and Stokes drift shear are largest [*Gnanadesikan and Weller*, 1995; *Polonichko*, 1997]. Since tidally driven shear is strongest near the ocean bottom, the near surface Eulerian shear is

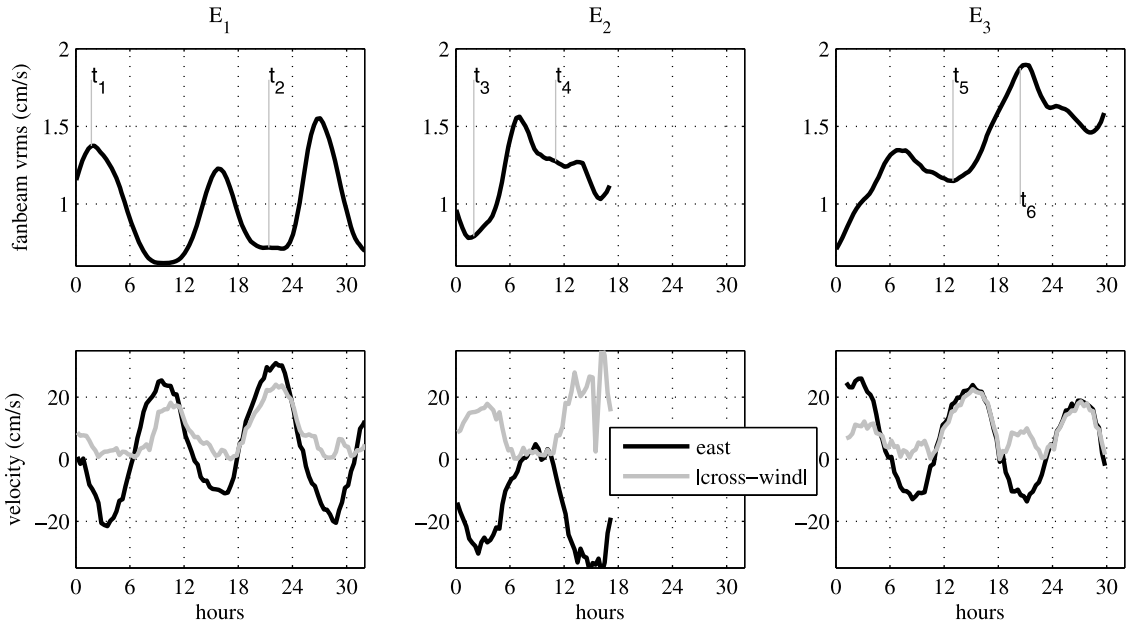

Figure 5. (top) Fan beam vrms varies with (bottom) tidal velocity. The east component of tidal current (black) and crosswind tidal current magnitude (gray) are shown. Tidal currents are from the bottom-mounted conventional ADCP (section 2.1.1) averaged from near surface (3 m, to avoid breaking wave effects) to middepth (8 m, to avoid bottom effects).

mainly driven by the wind stress. This suggests that LC convergence zones are roughly aligned with the wind and wave directions, which do not differ by more than 45° for the analysis events. Assuming that the beam with the strongest vrms signal is nearly orthogonal to LC convergence zones, i.e., approximately crosswind, the observed attenuation on tidal time scales may be due to crosswind tidal currents.

[22] Figure 5 shows fan beam vrms and observed tidal currents from the bottom-mounted conventional ADCP for all three analysis periods. For a typical crosswind tidal current of ~0.2 m/s and organized LC cells with a scale of $L/H \sim 3$ (section 3.2), the vrms instrument attenuation is only about 10%, i.e., significantly smaller than the observed tidal modulation, which can exceed 50% during some of the analysis periods. The fan beam vrms tidal modulation is particularly striking for event E1 when wind and wave conditions are fairly steady (see Figure 1), yet the vrms value varies significantly with vrms minima corresponding to crosswind current maxima. The tidal modulation is also evident during events E2 and E3 as the wind and wavefields develop. Nevertheless, local vrms minima roughly coincide with crosswind current maxima. During both E2 and E3 the general vrms trend is increasing with wind and waves for the first few hours, consistent with a decline in the turbulent Langmuir number that is associated with strengthening of wave forcing (compare with Figures 1 and 4). However, the vrms dips at t_3 and t_5, close to the time when crosswind tides reach a local maximum.

[23] This observed fan beam vrms tidal modulation cannot be explained by instrumentation attenuation alone. The occurrence of low vrms during relatively large crosswind currents suggests that crosswind flows influence LC dynamics.

3.2. Time-Range Velocity Anomalies

[24] Our results indicate that the observed modulation of fan beam vrms can be understood as a weakening of LC strength as the magnitude of crosswind tidal currents increases. Inspection of spatially resolved crosswind surface velocity anomalies v' suggests that LC also has smaller spatial scale and is less coherent during times with strong crosswind currents (Figure 6).

[25] Without strong crosswind flows (times t_1, t_4, t_6) banded coherent structures of surface divergence and convergence regions are apparent. The observed LC length scale is between 40 to 60 m, i.e., a typical horizontal length scale is around three times the water depth, which is consistent with previous observations of horizontal length scales between three to six times the water depth [*Gargett and Wells*, 2007].

[26] These results are in stark contrast to times t_2 and t_3 when the crosswind flow was around 20 cm/s and the wave forcing was relatively weak (larger turbulent Langmuir number, La_t). Neither of these observations indicate the presence of large-scale coherent features and the location of surface convergence and divergence regions appears more randomly with less organized features.

[27] At t_5, on the other hand, with a similarly strong crosswind flow, but larger wave forcing (smaller La_t), coherent structures are present. However, v' is smaller compared to the case without crosswind flow (t_6). This suggests that vrms depends on La_t and that crosswind mean flows are less effective in distorting LCs for relatively small La_t.

4. Mechanisms: LC Distortion by Crosswind Tidal Shear

[28] Tidal currents result in Eulerian mean shear and associated turbulence generation. The interactions of the

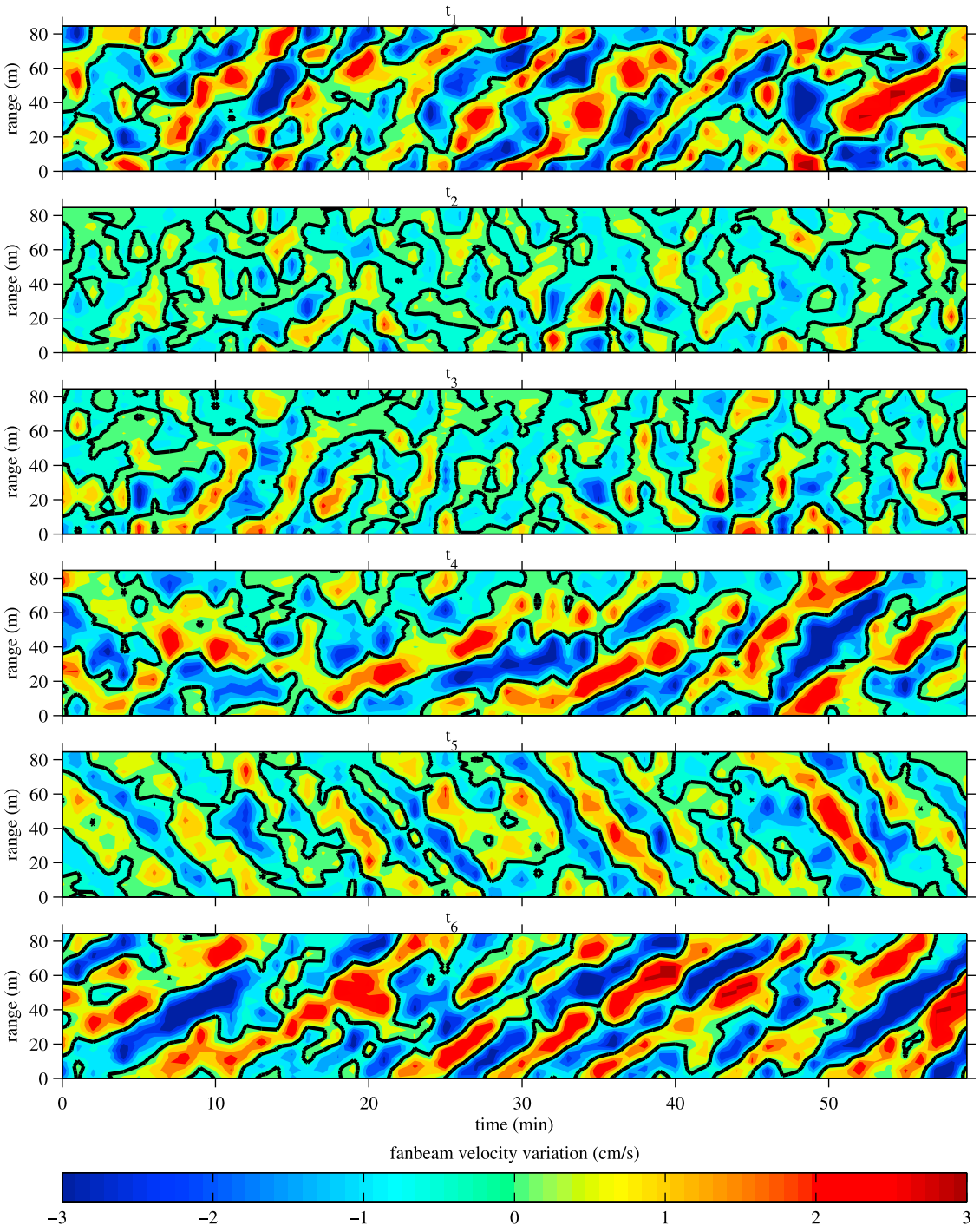

Figure 6. Fan beam velocity variations. Times t_i are also shown in Figure 4.

Eulerian mean shear and small-scale turbulence with the surface wavefield, in turn, are all expected to affect LC generation. Clearly, a comprehensive investigation of this problem is beyond the scope of our study. However, we hypothesize two mechanisms to explain the observed relationship between vrms and crosswind tidal currents.

[29] Crosswind tidal shear, which varies over a tidal cycle, plays a key role in both mechanisms. During times with relatively weak fan beam vrms, coinciding with relatively large crosswind mean flow, crosswind shear is generally also larger, e.g., at times t_2, t_3 and t_5 (Figure 7). Because the measurements are noisy, it is useful to examine the time-averaged profiles for significant crosswind tidal velocities during all three analysis periods (gray lines in Figure 7). On average, the crosswind shear is weak in the upper half of the water column and continuously increases to middepth and

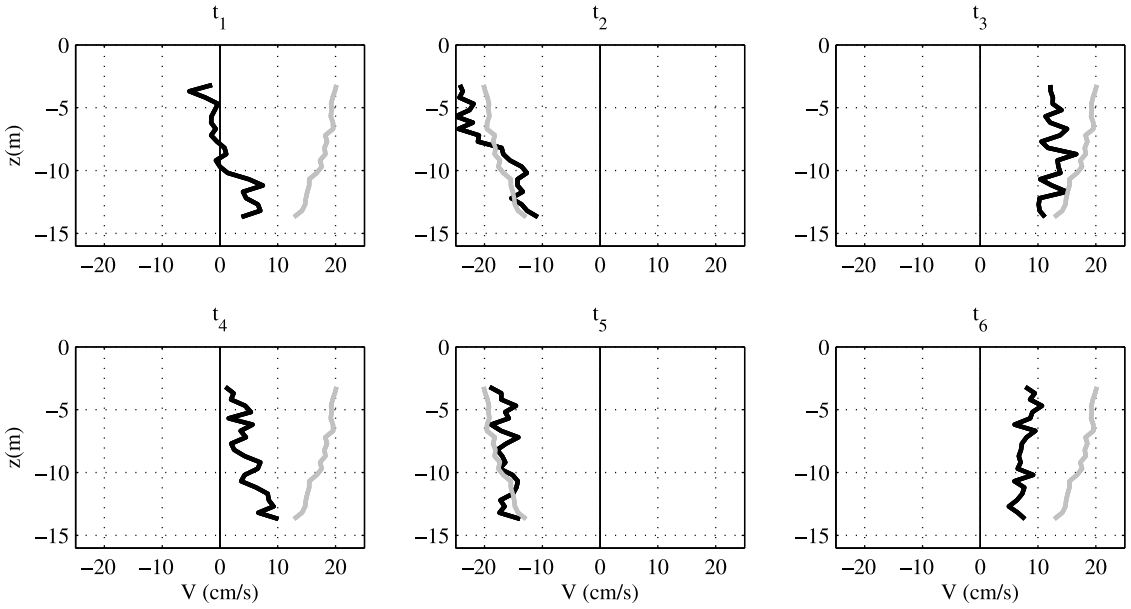

Figure 7. Observed hourly averaged crosswind tidal velocity profiles from a bottom-mounted conventional ADCP (black) for times t_i shown in Figure 4. The crosswind velocity profile averaged over all three analysis periods for crosswind velocities >15 cm/s provides a reference for comparison (gray).

reaches a maximum close to the bottom. This average profile, however, hides variable shear structure at any given instant. E.g., significant shear is present at middepth at t_2, while at t_5 observed $V(z)$ is approximately homogeneous, so that shear is mainly located close to the bottom. As discussed below, different shear structure might involve different mechanisms contributing to LC distortion.

[30] To understand the effects of crosswind flow on LC, it is important to keep in mind that LC convergence zones are roughly aligned with the wind (see discussion above) and that LC in a shallow ocean span the whole water column. Let a horizontal length and velocity scale be L and v_{LC}, respectively, and a vertical length and velocity scales be H and $(H/L)v_{LC}$ (by continuity), respectively. A typical LC time scale is then $T_{LC} \sim L/v_{LC} = H/[(H/L)v_{LC}]$.

4.1. Cell Shearing

[31] Because of the flow geometry, crosswind tidal shear will lead to differential advection across the cell (Figure 8), causing cell distortion. Furthermore, the crosswind flow results in a relative transverse motion of bottom and surface boundary layers, which both play important dynamical roles in shallow water LCs [*Gargett et al.*, 2004]. If this distortion is "strong", crosswind tidal flows may obstruct LC generation. A measure of the differential velocity between the bottom and top of the cell is $\frac{\partial V}{\partial z} H$. Strong distortion can

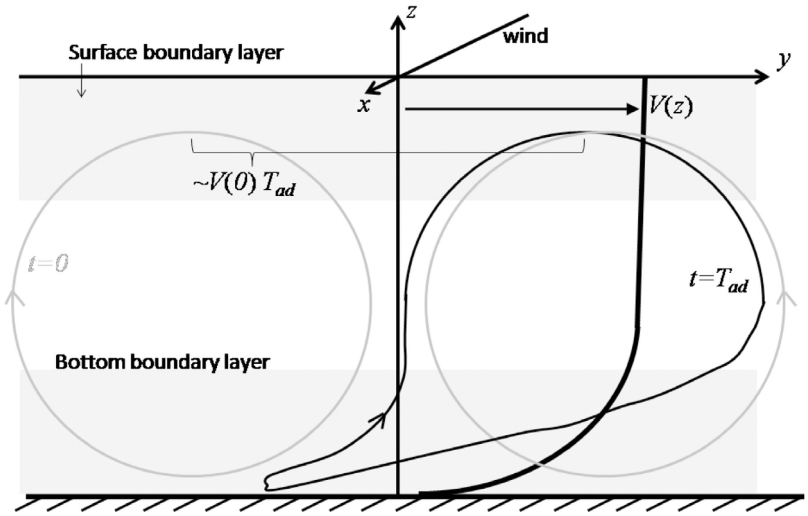

Figure 8. Sketch of LC distortion by crosswind mean flow V due to cell shearing.

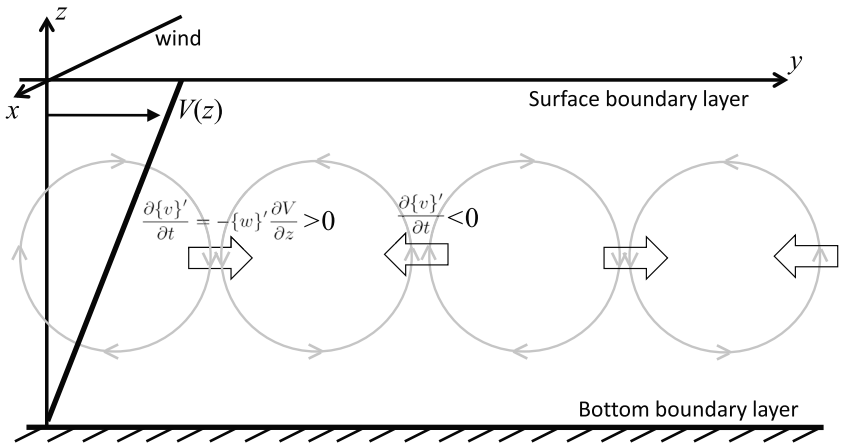

Figure 9. Sketch of LC distortion by crosswind mean flow V by attraction of downwelling and upwelling regions.

occur after the advective time scale, when the top of the cell is displaced by L

$$T_{ad} \sim \frac{L}{H}\left(\frac{\partial V}{\partial z}\right)^{-1}. \tag{5}$$

This advective time scale must be comparable or smaller than the turnover time scale of the LC cell T_{LC} in order to distort significantly the cell

$$\frac{T_{ad}}{T_{LC}} = \frac{L}{H}\frac{v_{LC}}{L}\left(\frac{\partial V}{\partial z}\right)^{-1} \leq \mathcal{O}(1). \tag{6}$$

Thus, LC distortion increases for greater cell aspect ratio (H/L), smaller LC surface convergence (v_{LC}/L), and larger crosswind shear ($\partial V/\partial z$). Extreme LC distortion is anticipated for $T_{ad} \ll T_{LC}$, which resembles the scaling applied in "rapid distortion theory" if $H \sim L$ and L, v_{LC} represent typical turbulent length and velocity scales, respectively [*Pope*, 2008].

[32] Let us next consider relevant time scales of LC and LC distortion. A velocity scale for LC, v_{LC}, likely involves the Stokes drift and the near surface water friction velocity due to wind u_{*wind} [*Plueddemann et al.*, 1996; *Smith*, 1998; *Li et al.*, 2005]. Since the Stokes drift and the water friction velocity are significantly correlated during the analysis events, we may estimate $v_{LC} \sim u_{*wind}$. Since a typical LC length scale for a single cell is related to the water depth, H, an LC time scale is estimated as $T_{LC} \sim H/u_{*wind}$. This time scale should be compared to the advective distortion time scale due to a sheared tidal current of magnitude V_0 at the surface and zero at the bottom, i.e., $T_{ad} \sim H/V_0$. Since a typical u_{*wind} scale is $u_{*wind} \sim 1$ cm/s and a typical tidal crosswind velocity scale is $V_0 \sim 10$ cm/s, LC experience significant distortion according to (6): $T_{ad}/T_{LC} \sim u_{*wind}/V_0 \sim 0.1$. Note that the estimate $v_{LC} \sim 1$ cm/s is consistent with the fan beam observations. Alternatively, one may estimate $\partial V/\partial z$ by a boundary layer scaling $\partial V/\partial z \sim u_{*bottom}/H$, where $u_{*bottom}$ is a crosswind bottom friction velocity. From (4) we find $\rho u_{*bottom}^2 \sim -H\,\partial P/\partial y$. For the simulations discussed below, whose crosswind mean flow is consistent with observations, we set $\rho^{-1}\,\partial P/\partial y = 7.3 \times 10^{-6}$ ms^{-2}, so that $u_{*bottom} \approx 1$ cm/s and $T_{ad}/T_{LC} \sim u_{*wind}/u_{*bottom} \sim 1$. Based on the relationship (6), we still anticipate that LC cells can be significantly distorted by the observed tidal currents.

4.2. Attraction of Upwelling and Downwelling Regions

[33] We evaluate the attraction mechanism by considering the local acceleration of the dominant LC velocity field due to advection by a mean crosswind tidal flow at middepth. The mean sheared crosswind velocity $V(z)$ causes advective crosswind accelerations/ decelerations

$$\frac{\partial\{v\}'}{\partial t} = -\{w\}'\frac{\partial V}{\partial z} - V\frac{\partial\{v\}'}{\partial y}, \tag{7}$$

where $\{u_i\}'$ denotes the dominant scale of the LC velocity field. Note that (7) is not the complete momentum equation for $\{v\}'$ because terms such as the Craik-Leibovich vortex force have been omitted. At mid depth $z = z_{mid}$, however, the Stokes drift shear, and thus the Craik-Leibvich vortex force, are negligible. Furthermore, upwelling and downwelling velocities are largest and $\partial\{v\}'/\partial y$ is small, so that

$$\left(\frac{\partial\{v\}'}{\partial t}\right)_{mid} \approx -(\{w\}')_{mid}\left(\frac{\partial V}{\partial z}\right)_{mid}. \tag{8}$$

For $(\partial V/\partial z)_{mid} > 0$ this implies that downwelling regions are accelerated along y, while upwelling regions are accelerated in the opposite direction (Figure 9). Eventually, as downwelling and upwelling regions approach one another, LC is unsustainable when convergence and divergence regions overlap.

[34] Scaling (8), upwelling and downwelling regions will overlap after a time scale

$$T_{ol} \sim \sqrt{\frac{L}{H}\frac{L}{v_{LC}}\left(\frac{\partial V}{\partial z}\right)^{-1}_{mid}} \tag{9}$$

The attraction of downwelling and upwelling regions is significant for

$$\frac{T_{ol}}{T_{LC}} = \sqrt{\frac{L}{H}\frac{v_{LC}}{L}\left(\frac{\partial V}{\partial z}\right)^{-1}_{mid}} \leq \mathcal{O}(1). \tag{10}$$

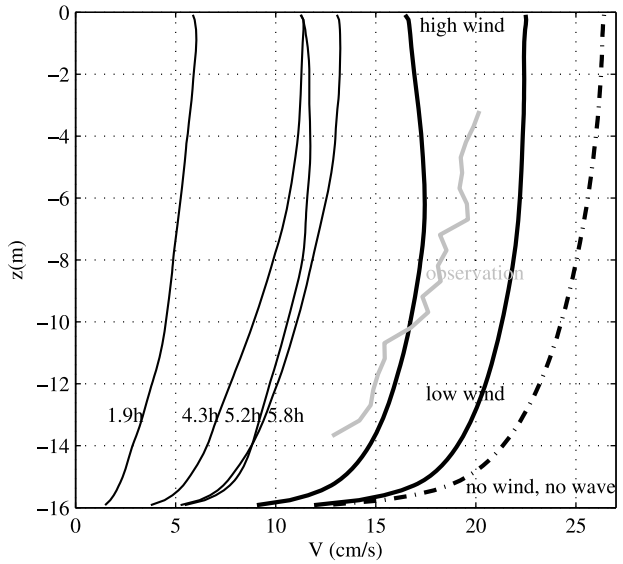

Figure 10. Horizontally averaged crosswind velocity profiles from the LES for approximately steady state (thick lines) and at the beginning of high wind spin-up at indicated hours after the crosswind pressure force is turned on (thin lines). The dash-dotted line shows a "background" mean crosswind velocity from the LES without wind and wave forcing. The observed crosswind velocity profile averaged over all analysis periods for crosswind velocities >15 cm/s provides a reference for comparison (gray line).

Except for the square root, this inequality is similar to the cell shearing condition for T_{ad}/T_{LC}. Note, however, that the local shear at mid depth is now critical rather than the "global" total shear across the whole cell.

[35] Thus, one requirement for the attraction mechanism is significant middepth shear, such as observed around t_2 (Figure 7). The cell shearing mechanism, on the other hand, might be more applicable around t_5, when middepth shear is weak (Figure 7). Note also that the two mechanisms are not exclusive, so that a combination of both may cause LC distortion.

5. Evidence Based on LES

[36] We perform four LES runs, in order to understand the sensitivities of LC on La_t and crosswind mean flow. A "low wind" case with U_{10} = 7 m/s, λ = 40 m, H_s = 0.75 m, so that La_t = 0.78 and a "high wind" case with U_{10} = 12 m/s, λ = 40 m, H_s = 1.5 m, so that La_t = 0.52. Both cases represent typical, observed coastal wind and wave conditions (see Figure 1 and discussion in section 2.1.2). Note that the shallow-water LC LES by *Tejada-Martínez and Grosch* [2007] was conducted for La_t = 0.7, suggesting that even for our "low wind" case (La_t = 0.78) LC could still be significant. This is confirmed by the observations (Figure 6, first panel) and the existence of Langmuir turbulence in the our LES conducted with La_t = 0.78. Sensitivity studies with $La_t \rightarrow \infty$ indicate fundamentally different turbulent characteristics. The wind stress is parameterized following *Large and Pond* [1981].

[37] For both high and low wind cases, we furthermore impose a crosswind pressure gradient that drives a mean crosswind flow with vertical shear (Figure 10). All simulations are run until turbulent fields reach an approximate statistically steady (stationary) state. The same initial condition is applied for all four simulations, based on a stationary low wind solution without mean crosswind pressure gradient.

[38] Once the simulations are stationary, simulated mean crosswind velocities with LC are close to the averaged observed profile (compare the thick black lines with gray line in Figure 10). Note that in the simulations shear is concentrated near the bottom, and the middepth shear is weaker than the observed mean profile. For weak middepth shear, we anticipate that the cell shearing mechanism is dominant and distorts LC cells. If wind and wave forcing are not included in the simulation (no LC), the crosswind velocities are notably larger than observed (Figure 10, dash-dotted line).

[39] Middepth shear is significant, however, for the first few hours after the crosswind pressure force is turned on (thin black lines Figure 7), which indicates that observed tidal currents do not reach a steady state. Because the initial condition is obtained from the fully developed LES solution without crosswind mean flow, fields are always fully developed during the "spin-up" with crosswind pressure force. To examine middepth shear, we will also briefly investigate simulations during this spin-up, when the shear

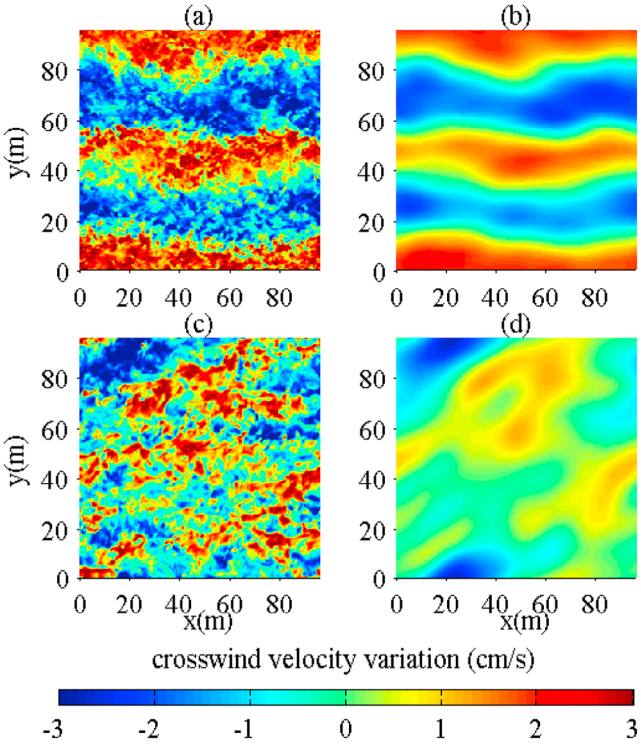

Figure 11. LES solution of v' for low wind case at z = −1.2 m (a, b) without and (c, d) with mean crosswind flow. Instantaneous snapshot (Figures 11a and 11c), 60 sec and spatial average similar to observational data processing (Figures 11b and 11d). Note same color range as in Figure 6.

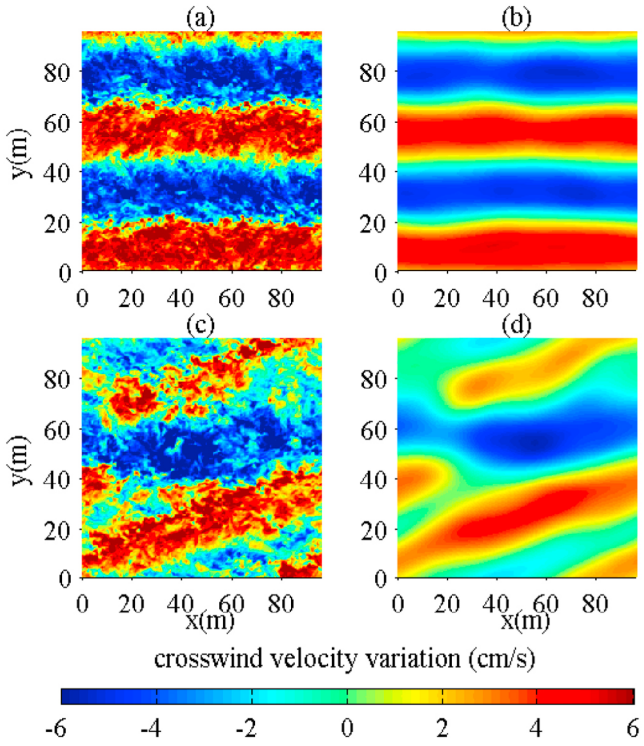

Figure 12. LES solution of v' for high wind case at $z = -1.2$ m (a, b) without and (c, d) with mean crosswind flow. Instantaneous snapshot (Figures 12a and 12c), 60 sec and spatial average similar to observational data processing (Figures 12b and 12d). Note different color range from Figure 11 because v' is significantly larger for the high wind case.

in the upper two third of the water column resembles the averaged observed profile.

[40] Crosswind velocity results are presented for $z = -1.2$ m approximately corresponding to the major depth response of the fan beam instrument (the main depth range response due to a variable bubble layer is about $z = -1.0$ m to $z = -2.3$ m).

5.1. Low Wind Case (Larger La_t)

[41] Imposed wind and wave conditions most closely resemble the observed wind event 1 (Figure 1).

5.1.1. Without Crosswind Flow

[42] Without crosswind mean flow the crosswind vrms at $z = -1.2$ m is vrms = 1.8 cm/s (vrms = 1.9 cm/s at $z = -1.0$ m and vrms = 1.4 cm/s at $z = -2.3$ m). Applying a similar averaging procedure as for the fan beam observations, the simulated fan beam vrms reduces to vrms = 1.3 cm/s (Figures 11a and 11b). Thus, although smaller scales are present (28% reduction of vrms), the majority of the crosswind velocity variations is due to larger-scale LC. The simulated crosswind velocity variations are quantitatively and qualitatively similar to the observed crosswind velocity variations (compare to t_1 in Figure 6).

5.1.2. With Crosswind Flow

[43] This time a large-scale pressure gradient is imposed to generate a volume averaged crosswind current of 21 cm/s, consistent with the largest observed crosswind current during event 1 (Figure 5, left). The crosswind vrms at $z = -1.2$ m is reduced to vrms = 1.5 cm/s (vrms = 1.5 cm/s at $z = -1.0$ m and vrms = 1.4 cm/s at $z = -2.3$ m), which is relatively close to the case without crosswind flow. However, applying a similar averaging procedure as for the fan beam observations, the simulated fan beam vrms reduces significantly to vrms = 0.7 cm/s (Figures 11c and 11d). This is because the majority of the crosswind velocity variations are due to relatively small-scale LC, suggesting that the large-scale flow pattern is disrupted (>50% reduction of vrms). Compared to the no crosswind mean flow case, the simulated fan beam vrms reduces by $1 - 0.007/0.013 = 46\%$, which is consistent with the vrms reduction observed in Figure 5 (left). The simulated crosswind velocity variations are quantitatively and qual-

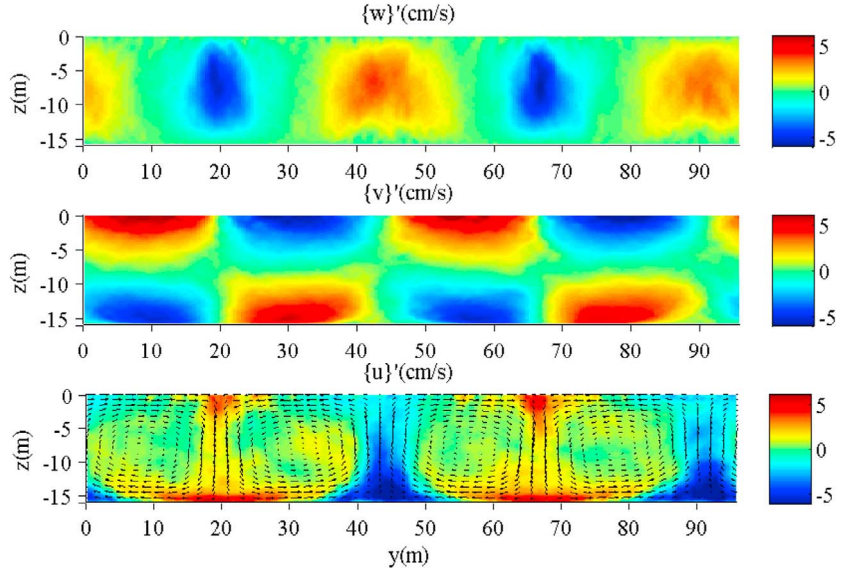

Figure 13. Along x averaged velocity deviations from horizontal mean just when the pressure gradient force is started at $t = 0$ h (i.e., without mean crosswind flow).

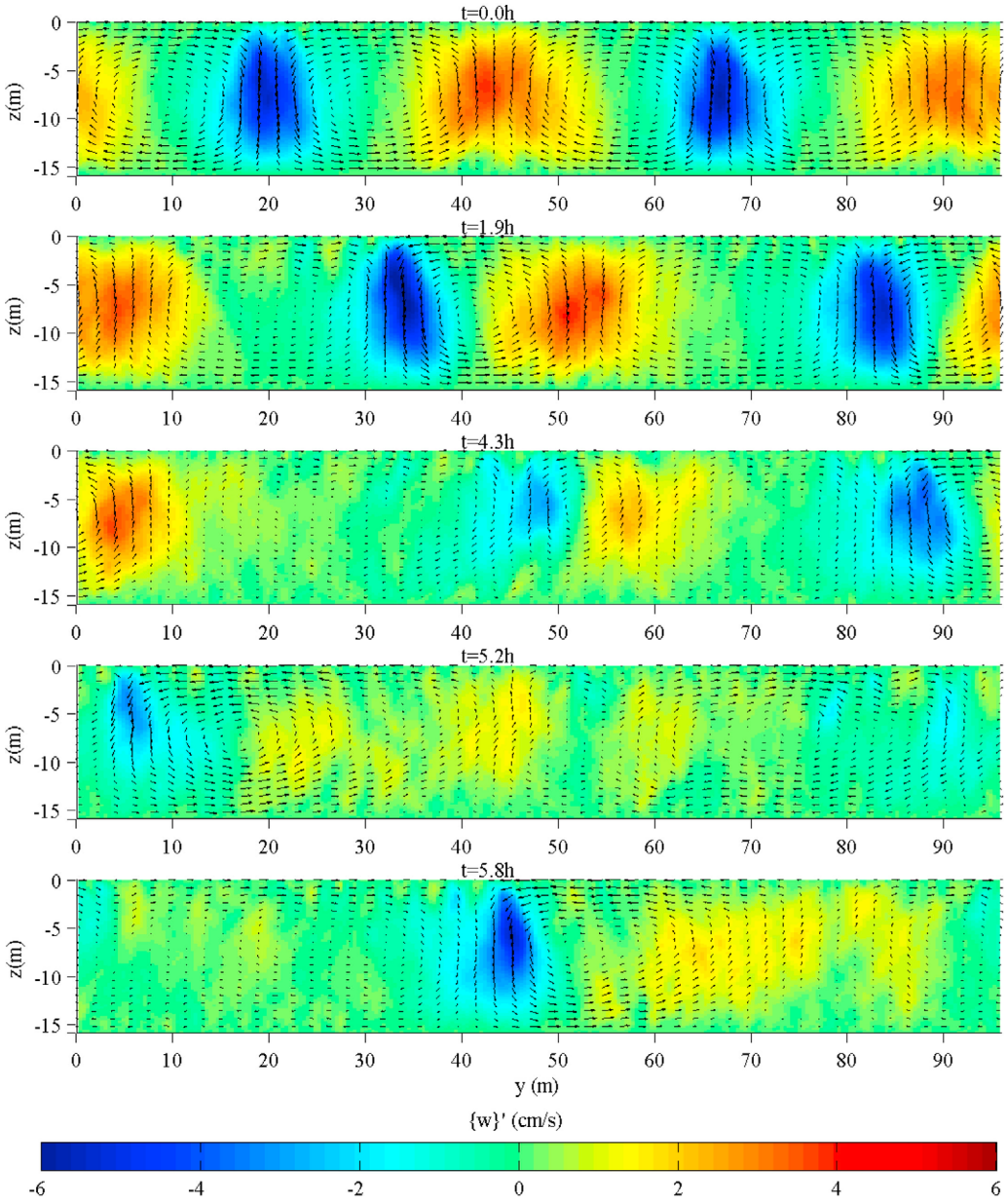

Figure 14. Along x averaged vertical velocity $\{w\}'$ at time t after the crosswind pressure gradient is turned on at $t = 0$ (compare Figure 13). Arrows indicate direction and relative magnitude of LC cell velocities. Note how downwelling and upwelling regions approach one another as expected from the "attraction of downwelling and upwelling regions mechanism."

itatively similar to the observed crosswind velocity variations (at t_2 in Figure 6). According to the scaling discussed in section 4, one estimate of the ratio of distortion to LC time scale is $v_{LC}/V_0 \approx 0.7/21 = 0.033 \ll 1$, so that we anticipate significant LC distortion. The simulated mean shear (Figure 10), is relatively small at middepth, suggesting that the cell-shearing mechanism might be more important in disrupting LC cells.

5.2. High Wind Case (Smaller La_t)

[44] Imposed wind and wave conditions most closely resemble the conditions observed near the end of wind events 2 and 3 (Figure 1). Note however, that observed wind and waves are developing, so that the observations represent different conditions from the stationary simulated conditions.

5.2.1. Without Crosswind Flow

[45] The simulated LC length scales are similar for low and high wind cases, but the high-wind case shows stronger convergence velocities with crosswind vrms at $z = -1.2$ m of vrms = 4.3 cm/s (vrms = 4.4 cm/s at $z = -1.0$ m and vrms = 3.5 cm/s at -2.3 m). The comparison of the normalized value vrms/u_* = 2.9 to the value found for the low wind case vrms/u_* = 2.1 suggests that La_t is a critical parameter in determining vrms, which is consistent with previous studies. Applying a similar averaging procedure as for the fan

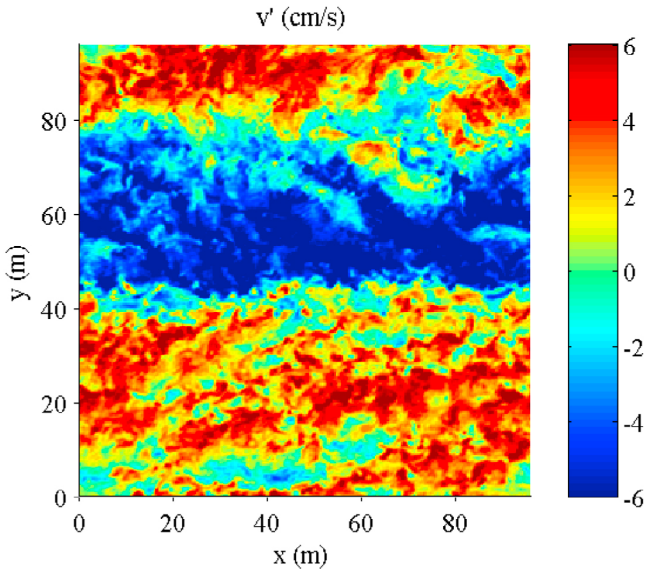

Figure 15. LES solution of v' for high wind case at z = 1.2 m during mean crosswind current spin-up after t = 5.6 h. Mean crosswind current is 0.11 m/s. During the spin-up from about t = 5 h to 8 h the dominant LC horizontal scale is 6 × H, rather than 3 × H as simulated for the cases without mean crosswind currents. Stationary state is approximately reached after 12 h LC scales vary irregularly then, as shown in Figures 12c and 12d. Note same color range as in Figure 12.

beam observations, the simulated fan beam vrms reduces to vrms = 3.5 cm/s (Figures 12a and 12b). This 19% reduction of vrms is less than for the smaller La_t case, suggesting that for greater La_t more crosswind velocity variations are due to larger-scale LC. Simulated crosswind velocity variations are qualitatively (coherent bands, scales) similar to the observed crosswind velocity variations (t_4, t_6 Figure 6). The simulated crosswind velocity variations, however, differ quantitatively from the observed crosswind velocity variations, most likely due to the fact that the observations are not stationary.

5.2.2. With Crosswind Flow

[46] The same large-scale pressure gradient is imposed as in the low wind case. Because of the enhanced turbulent mixing in high winds, the simulated vertically averaged crosswind current is reduced to 16 cm/s, but is still comparable to observed crosswind mean flows (Figure 5, middle and right). Note that the reduction in V generally implies a decrease in shear also. Thus enhanced wind, decreased La_t, and reduced V all result in a decrease of the LC time scale T_{LC} relative to the distortion time scale. By the scaling (6) or (8), we thus anticipate reduced LC cell distortion compared to the low wind case.

[47] The crosswind vrms at z = −1.2 m is vrms = 3.5 cm/s (vrms = 3.6 cm/s at z = −1.0 m and vrms = 2.9 cm/s at z = −2.3 m), which is as in the low wind case relatively close to the case without crosswind flow. Applying a similar averaging procedure as for the fan beam observations, the simulated fan beam vrms reduces to vrms = 2.5 cm/s (Figures 12c and 12d), so that smaller scales are present (29% reduction of vrms), but the majority of the crosswind velocity variations is due to larger-scale LC.

[48] Again, applying the scaling from section 4, we may estimate the ratio $v_{LC}/V_0 \approx 2.5/16 = 0.16$, which is an order of magnitude larger than for the low wind case. These results suggest that for the high wind case, the mean crosswind flow is indeed less effective in distorting larger-scale LC, which is qualitatively consistent with the observations. For times t_2, t_3, and t_5 significant mean crosswind flow is present. Only for time t_5 when La_t is relatively small are banded LC structures present. Coherent bands and scales of the simulated crosswind velocity variations are similar to the observed crosswind velocity variations (compare t_5 from Figure 6 with Figure 12d). However, the simulated crosswind velocity variations differ quantitatively from the observed crosswind velocity variations, probably because the observations are not stationary.

5.3. Direct Evidence for Attraction Mechanisms

[49] We investigate the initial development for the high wind case just after the pressure gradient force is turned on and crosswind mean currents are allowed to develop (Figures 13 and 14). The initial fields are from the stationary high wind case without mean crosswind flows (Figure 13), which closely resemble the shallow water LC simulations from *Tejada-Martínez and Grosch* [2007]. As in the work by *Tejada-Martínez and Grosch* [2007], the fields are averaged along x, which is viable because LCs are initially well organized and aligned with the wind direction. As the mean crosswind current accelerates, downwelling and upwelling regions approach one another as expected from the "attraction mechanism" and weaken (Figure 14) until w due to LC are very weak after about 5 h. Finally a new LC cell is formed with smaller aspect ratio L/H which is more stable for fixed horizontal convergence v_{LC}/L and fixed shear $\partial V/\partial z$ according to (8) (Figure 15 and Figure 14 (bottom)).

[50] Kinematically, LC cells with horizontal scales, L, that are much larger than vertical scales, H, are less affected by advective crosswind distortion. It is therefore conceivable that mean crosswind flow can result in LC cells with $L \gg H$, as simulated here. However, if such large scale were present in the observations, these might not have been detectable by the fan beam, because the limited along beam extent implies that spatial scales significantly longer than 85 m are undetectable (see description in section 2.1.3).

[51] Note that the cell shearing mechanism is more challenging to illustrate directly based on LES because turbulent fields are already irregular. It is insightful to examine normalized autocovariance functions based on LES solution of v', which clearly decrease with crosswind flow for the low-wind case (Figure 16), suggesting weaker LC activity with mean crosswind flow. For the high-wind case, the autocovariance still decreases with crosswind flow, but the decrease is relatively weak. Consistent with the results from section 5.2, the crosswind flow is less effective in distorting larger-scale LC for the high wind case (which coincides with smaller La_t). Furthermore, the scaling (6) and the simulated destruction of LC by crosswind mean flow provides some evidence for the existence of the shearing mechanism. Likely, in the presence of midlevel crosswind

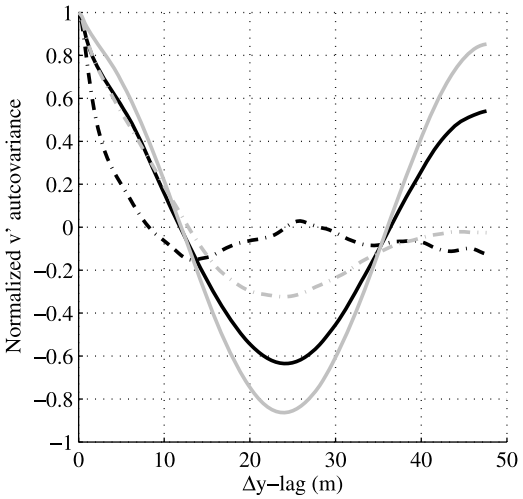

Figure 16. Normalized autocovariance functions based on LES solutions of v' at $z = -1.2$ m (see Figures 11 and 12) for low (black) and high (gray) wind cases without (solid line) and with (dash-dotted line) mean crosswind flow. The lag Δy is for the crosswind direction.

shear the attraction mechanism acts together with the cell shearing mechanism.

[52] Our LES results suggest that LC is obstructed over time scales shorter than the tidal time scale. To investigate the time scale of LC formation/ reorganization we have conducted two additional LES sensitivity experiments (results not shown). For the first simulation, the crosswind pressure gradient varied sinusoidally to generate an oscillating tidal current. For the second simulation, the crosswind mean flow was suddenly stopped at time t = 5.2 h (high wind case see Figure 14). Results of both simulations indicate that the LC formation/ reorganization time scale is smaller than a tidal time scale. Thus, the proposed mechanisms are consistent with the observed vrms tidal modulation.

6. Summary and Conclusions

[53] Based on observations, simple conceptual models, and large eddy simulations (LES) we illustrate that strong crosswind tidal currents distort Langmuir circulation (LC) in a shallow ocean. Observations were obtained during the CBLAST-low experiment and included measurements of wind, wave, and tide conditions. Special purpose "fan beam" instrumentation revealed time series of near surface convergence velocities due to LC as function of instrument beam range. In the presence of strong crosswind tidal currents, observed LC convergence velocities are weaker and less coherent.

[54] We hypothesize two mechanisms by which crosswind tidal shear significantly distorts LC cells. The first mechanism involves cell shearing due to differential advection across the whole cell. For the second mechanism, we propose that downwelling currents advect the sheared crosswind current, leading to an acceleration of downwelling regions in the direction of the crosswind current. Similarly, upwelling regions will be accelerated against the crosswind current, ultimately resulting in the attraction of downwelling and upwelling regions. Unlike the cell shearing mechanism, for which shear across the whole cell is important, the attraction mechanism requires significant shear at middepth, where upwelling and downwelling velocities are largest. A scaling analysis suggests that for both mechanisms the distortion increases with greater shear, smaller LC surface velocity convergence, and greater cell aspect ratio (vertical to horizontal scale). This scaling is qualitatively consistent with the results obtained from the observations and LES.

[55] An idealized shallow-water LES model was designed to capture key aspects of the observations and to investigate the effects of crosswind shear on LC. We performed a "low" and "high" wind simulation (coinciding with a larger and smaller turbulent Langmuir number, La_t, respectively) with and without mean crosswind currents; the latter are driven by an imposed crosswind pressure gradient. The simulated horizontal LC scales are roughly consistent with the observations (3–4 times the water depth). As in the observations, for larger La_t (weaker wave forcing) LC cells are unsustainable in the presence of strong crosswind tidal flow, while coherent (LC) surface convergence velocities are present but weaker for smaller La_t (larger wave forcing).

[56] A more complete, quantitative evaluation of changes in the momentum and energy balances associated with the shearing and attraction mechanisms could be undertaken using the output of the LES simulations. However, separating mean, LC and "turbulent" components in order to diagnose terms in the momentum and energy equations is a substantial task [e.g., *Skyllingstad et al.*, 2000; *Kukulka et al.*, 2010]. Here we have focused on establishing the plausibility of the two LC distortion mechanisms based on comparison of observations and LES results.

[57] Our results imply that the scaling of LC in a coastal ocean differs from that in the open ocean. In particular, the presence of crosswind shear may disrupt LC and contribute to the small LC aspect ratios (vertical to horizontal LC scale) found in the CBLAST observations. Our results provide a particular example of Eulerian mean currents that strongly affect LC. Since Eulerian mean currents generated by tides do not scale with wind properties, one may expect that LC properties generally do not scale with wind and wave characteristics alone. Finally, we note that the proposed attractor mechanism is "nonlinear" as crosswind flow perturbations advect vertical LC currents. Such nonlinear behavior might render a linear stability analysis for LC inadequate in the presence of cross-cell shear.

[58] **Acknowledgments.** This research was supported by the Office of Naval Research through grant N00014-06-1-0178 (A.P., J.T.). Author T.K. received support from Faculty Startup Funds of the University of Delaware College of Earth, Ocean, and Environment. We would like to thank two anonymous reviewers for constructive criticism that improved the manuscript.

References

Churchill, J. H., A. J. Plueddemann, and S. M. Faluotico (2006), Extracting wind sea and swell from directional wave spectra derived from a bottom-mounted ADCP, *Tech. Rep. 2006-13*, 34 pp., Woods Hole Oceanogr. Inst., Woods Hole, Mass.

Craik, A. D. D., and S. Leibovich (1976), A rational model for Langmuir circulations, *J. Fluid Mech.*, *73*, 401–426.

Deardorff, J. W. (1973), The use of subgrid transport equations in a three-dimensional model of atmospheric turbulence, *J. Fluids Eng.*, *95*, 429–439.

Edson, J., et al. (2007), The coupled boundary layers and air-sea transfer experiment in low winds, *Bull. Am. Meteorol. Soc.*, *88*(3), 341–356.

Gargett, A. E., and J. R. Wells (2007), Langmuir turbulence in shallow water. Part 1. Observations, *J. Fluid Mech.*, *576*, 27–61, doi:10.1017/S0022112006004575.

Gargett, A. E., J. Wells, A. E. Tejada-Martinez, and C. E. Grosch (2004), Langmuir supercells: A mechanism for sediment resuspension and transport in shallow seas, *Science*, *306*, 1925–1928.

Gerbi, G. P., J. H. Trowbridge, E. A. Terray, A. J. Plueddemann, and T. Kukulka (2009), Observations of turbulence in the ocean surface boundary layer: Energetics and transport, *J. Phys. Oceanogr.*, *39*, 1077–1096.

Gnanadesikan, A., and R. Weller (1995), Structure and instability of the Ekman Spiral in the presence of surface gravity waves, *J. Phys. Oceanogr.*, *25*, 3148–3171.

Harcourt, R. R., and E. A. D'Asaro (2008), Large-eddy simulation of Langmuir turbulence in pure wind seas, *J. Phys. Oceanogr.*, *38*, 1542–1562.

Kukulka, T., A. J. Plueddemann, J. H. Trowbridge, and P. P. Sullivan (2010), Rapid mixed layer deepening by the combination of Langmuir and Shear instabilities: A case study, *J. Phys. Oceanogr.*, *40*, 2381–2400.

Large, W. G., and S. Pond (1981), Open ocean momentum flux measurements in moderate to strong winds, *J. Phys. Oceanogr.*, *11*, 324–336.

Leibovich, S. (1983), The form and dynamics of Langmuir circulations, *Annu. Rev. Fluid Mech.*, *15*, 391–427.

Li, M., L. Sanford, and S.-Y. Chao (2004), Effects of time dependence in unstratified tidal boundary layers: Results from large eddy simulations, *Estuarine Coastal Shelf Sci.*, *62*(1–2), 193–204, doi:10.1016/j.ecss.2004.08.017.

Li, M., C. Garrett, and E. Skyllingstad (2005), A regime diagram for classifying turbulent large eddies in the upper ocean, *Deep Sea Res., Part I*, *52*(2), 259–278.

McWilliams, J. C., P. P. Sullivan, and C.-H. Moeng (1997), Langmuir turbulence in the ocean, *J. Fluid Mech.*, *334*, 1–30.

Nezu, I. (2005), Open-channel flow turbulence and its research prospect in the 21st century, *J. Hydraul. Eng.*, *131*(4), 229–247, doi:10.1061/(ASCE)0733-9429(2005)131:4(229).

Plueddemann, A., J. Smith, D. Farmer, R. Weller, W. Crawford, R. Pinkel, S. Vagle, and A. Gnanadesikan (1996), Structure and variability of Langmuir circulation during the surface waves processes program, *J. Geophys. Res.*, *101*(C2), 3525–3543.

Plueddemann, A. J., E. A. Terray, and R. Merewether (2001), Design and performance of a self-contained fan-beam ADCP, *IEEE J. Oceanic Eng.*, *26*, 252–258.

Polonichko, V. (1997), Generation of Langmuir circulation for nonaligned wind stress and the stokes drift, *J. Geophys. Res.*, *102*(C7), 15,773–15,780.

Polton, J. A., and S. E. Belcher (2007), Langmuir turbulence and deeply penetrating jets in an unstratified mixed layer, *J. Geophys. Res.*, *112*, C09020, doi:10.1029/2007JC004205.

Pope, S. B. (2008), *Turbulent Flows*, 5th ed., 771 pp., Cambridge Univ. Press, Cambridge, U. K.

Skyllingstad, E. D., W. D. Smyth, and G. B. Crawford (2000), Resonant wind-driven mixing in the ocean boundary layer, *J. Phys. Oceanogr.*, *30*, 1866–1890.

Smith, J. A. (1989), Doppler sonar and surface waves: Range and resolution, *J. Atmos. Ocean. Technol.*, *6*, 680–696.

Smith, J. A. (1992), Observed growth of Langmuir circulation, *J. Geophys. Res.*, *97*(C4), 5651–5664.

Smith, J. A. (1998), Evolution of Langmuir circulation during a storm, *J. Geophys. Res.*, *103*(C6), 12,649–12,668.

Sullivan, P. P., J. C. McWilliams, and C.-H. Moeng (1994), A subgrid-scale model for large-eddy simulation of planetary boundary-layer flows, *Boundary Layer Meteorol.*, *71*, 247–276.

Tejada-Martínez, A. E., and C. E. Grosch (2007), Langmuir turbulence in shallow water. Part 2. Large-eddy simulation, *J. Fluid Mech.*, *576*, 63–108.

Thorpe, S. A. (2004), Langmuir circulation, *Annu. Rev. Fluid Mech.*, *36*, 55–79.

Zedel, L., and D. Farmer (1991), Organized structures in subsurface bubble clouds: Langmuir circulation in the open ocean, *J. Geophys. Res.*, *96*(C5), 8889–8900.

T. Kukulka, Physical Ocean Science and Engineering, College of Earth, Ocean, and Environment, University of Delaware, 211 Robinson Hall, Newark, DE 19716, USA. (kukulka@udel.edu)

A. J. Plueddemann, Department of Physical Oceanography, Woods Hole Oceanographic Institution, MS 29, 360 Woods Hole Rd., Woods Hole, MA 02543, USA. (aplueddemann@whoi.edu)

P. P. Sullivan, National Center for Atmospheric Research, PO Box 3000, Boulder, CO 80307, USA. (pps@ucar.edu)

J. H. Trowbridge, Department of Applied Ocean Physics and Engineering, Woods Hole Oceanographic Institution, 98 Water St., Woods Hole, MA 02543, USA. (jtrowbridge@whoi.edu)